



HAL
open science

Self-phase modulation and four-wave mixing in a chalcogenide ridge waveguide

Enguerran Delcourt, Nessim Jebali, Loïc Bodiou, Marion Baillieul, Emeline Baudet, Jonathan Lemaitre, Virginie Nazabal, Yannick Dumeige, Joël Charrier

► **To cite this version:**

Enguerran Delcourt, Nessim Jebali, Loïc Bodiou, Marion Baillieul, Emeline Baudet, et al.. Self-phase modulation and four-wave mixing in a chalcogenide ridge waveguide. *Optical Materials Express*, 2020, 10 (6), pp.1440-1450. 10.1364/OME.393535. hal-02879002

HAL Id: hal-02879002

<https://hal.science/hal-02879002>

Submitted on 23 Jun 2020

HAL is a multi-disciplinary open access archive for the deposit and dissemination of scientific research documents, whether they are published or not. The documents may come from teaching and research institutions in France or abroad, or from public or private research centers.

L'archive ouverte pluridisciplinaire **HAL**, est destinée au dépôt et à la diffusion de documents scientifiques de niveau recherche, publiés ou non, émanant des établissements d'enseignement et de recherche français ou étrangers, des laboratoires publics ou privés.



Self-phase modulation and four-wave mixing in a chalcogenide ridge waveguide

ENGUERRAN DELCOURT,¹ NESSIM JEBALI,¹ LOÏC BODIQU,¹ 
MARION BAILLIEUL,² EMELINE BAUDET,² JONATHAN LEMAITRE,¹
VIRGINIE NAZABAL,²  YANNICK DUMEIGE,¹ AND JOËL
CHARRIER^{1,*}

¹Univ Rennes, CNRS, Institut FOTON, UMR-CNRS 6082, BP80518, F-22305 Lannion Cedex, France

²Univ Rennes, CNRS, ISCR (Institut des Sciences Chimiques de Rennes) UMR 6226, F-35000 Rennes, France

*joel.charrier@univ-rennes1.fr

Abstract: Third order optical nonlinear effects relying on the instantaneous Kerr effect are investigated in a straight chalcogenide ridge waveguide. The sample consists of a GeSbSe film deposited on a thermally oxidized silicon substrate. Ridge waveguides were processed using photolithography and dry etching techniques. From a 1.1 cm long integrated GeSbSe device, self-phase modulation with a maximum nonlinear phase shift of 2.02π for a peak power of 15.8 W and four-wave mixing with an external conversion efficiency of -42.6 dB for a pump power of 28 mW are demonstrated. Experimental results show a good agreement with calculations.

© 2020 Optical Society of America under the terms of the [OSA Open Access Publishing Agreement](#)

1. Introduction

Photonic integrated circuits (PICs) are of key importance as they offer compelling performance advances in terms of bandwidth, flexibility, and energy consumption which can underpin the modern telecommunications networks. Nonlinear optics offers an all-optical alternative to optical-electrical-optical based solutions and may offer competitive advantages as data densities and rates continue to increase. The main idea behind PICs is to gather within a single monolithic chip a variety of functions which are all required to provide, all-optically, some complex processing tasks. Different optical nonlinear processes such as third-harmonic generation, self-phase modulation (SPM), cross-phase modulation and four-wave mixing (FWM) have been used to implement a broad range of functionalities dedicated to all-optical signal processing. By far, the most common used nonlinear optical effect is FWM which occurs when two pump photons are annihilated to create two photons at frequencies shifted toward the blue and red sides. Applying different pumping schemes, FWM in an integrated platform have been demonstrated for providing various applications, such as signal regeneration [1], wavelength channel conversion [2], and logic operations [3], all of which could be modulation-format transparent and compatible with coherent communications. The quest for all-optical components has naturally targeted materials with extremely large nonlinearity including semiconductors (Si, III-V) [4–6], chalcogenide glasses [7] and polymers [8], but also low-loss platforms (silicon dioxide [9] and silicon nitride [10,11]). A lot of efforts have been made to develop nonlinear photonic devices on the silicon platform; even though promising results have been shown, this platform suffers from free-carrier dispersion and absorption through two-photon absorption (TPA) process which leads to a limitation of the operational speed of devices. The intrinsic limitations of silicon have motivated the development of alternative integrated nonlinear platforms that are still compatible with silicon photonics in order to access broader transparency window (visible, UV or mid-IR), suppress the nonlinear absorption and achieve ultra-low losses.

Chalcogenide glasses (ChG) have attracted significant attention in recent years as a major technological platform for all-optical devices [12]. They are amorphous materials containing as a major constituent one or more of the chalcogen elements from group VIA of the periodic table (i.e. Sulphur (S), Selenium (Se), Tellurium (Te), but excluding oxygen (O)) covalently bonded to other elements such as arsenic (As), germanium (Ge), antimony (Sb), gallium (Ga), silicon (Si) and phosphorus (P). Therefore, it is possible to formulate them differently to meet different demands for refractive index, transmission range, hardness, band-edge energy, optical nonlinearity. These specific chemical compositions can yield glasses with unique and striking optical properties that make them compelling for near- and mid-infrared applications [13]. The instantaneous third-order (Kerr) nonlinearity, combined with strong confinement and dispersion engineering achievable in waveguide devices, make ChG glasses a promising platform for all-optical signal processing [14–16]; the absence of free carriers or two-photon absorption insures that the nonlinearity is near-instantaneous and dispersive. The intrinsic transparency window of ChGs, which includes much of the molecular fingerprint region of 2–25 μm , makes them also attractive for spectroscopy and optical sensing [17].

This paper reports on efficient nonlinear processes highlighted through the demonstration of SPM and FWM in a 1.1 cm long straight GeSbSe ridge waveguide (on SiO_2) that was geometrically optimized to yield small effective area and concomitantly, large nonlinear coefficient. Spectral broadening induced by SPM is observed, the related experimental results are fitted using a numerical model in order to estimate the nonlinear index. FWM in CW regime is also reported. Conversion efficiency measurements are compared to theory with a reasonable agreement.

2. Sample preparation

The geometry of the GeSbSe waveguide is illustrated in Fig. 1(a). The waveguide dimensions were chosen in a way to ensure a single-mode propagation. Selenide glass targets with a nominal composition of $\text{Ge}_{12.5} \text{Sb}_{25} \text{Se}_{62.5}$ named Se_6 , was prepared using the conventional melting and quenching techniques from commercial elemental precursors of high purity (5N) [18]. Using radio frequency (RF) magnetron sputtering, a 400 nm thick film of Se_6 ($n=2.88$ @ 1.55 μm) was then deposited onto silicon wafers with 2 μm of thermal oxide ($n=1.44$ @ 1.55 μm) [19]. A ridge waveguide with 600 nm width was then patterned using a standard i-line photolithographic process (MJB4 Suss Microtech mask aligner) and followed by a dry etching procedure at low pressure (Corial 200IL) combining reactive ion etching (RIE) and inductively coupled plasma (ICP) etching (5 sccm CHF_3 , 5 mTorr, 75 W ICP, 25 W RF). These optimized etching conditions enable anisotropic etching, with vertical sidewalls desirable for fabrication of rectangular waveguides. The fabrication procedures are summarized in Fig. 2. An image of the sample taken by scanning electron microscopy (SEM) is shown in Fig. 1(b). Waveguide with vertical sidewalls are achieved with a good anisotropy; showing the high quality of the fabrication procedures. Figure 1(c) shows the simulated field distribution of the fundamental TE-mode at a wavelength of 1550 nm. The nonlinear effective area is calculated for different geometrical parameters (width W and height H) by using the following equation [20]:

$$A_{\text{eff}, \text{NL}} = \frac{Z_0^2}{n_{\text{core}}^2} \frac{\left| \iint_{D_{\text{tot}}} \{E \times H\} \cdot e_z \, dx dy \right|^2}{\iint_{D_{\text{core}}} |E|^4 \, dx dy} \quad (1)$$

where Z_0 is the free space impedance, n_{core} is the refractive index of the core, D_{core} is the nonlinear core domain and e_z is the unit vector along z -direction. E and H represent the electric and magnetic field, respectively.

Figure 1(d) displays the obtained effective nonlinear area as a function of the core waveguide width and height. The GeSbSe waveguide with a width of 600 nm and height of 400 nm results in a small effective nonlinear interaction area of 0.13 μm^2 .

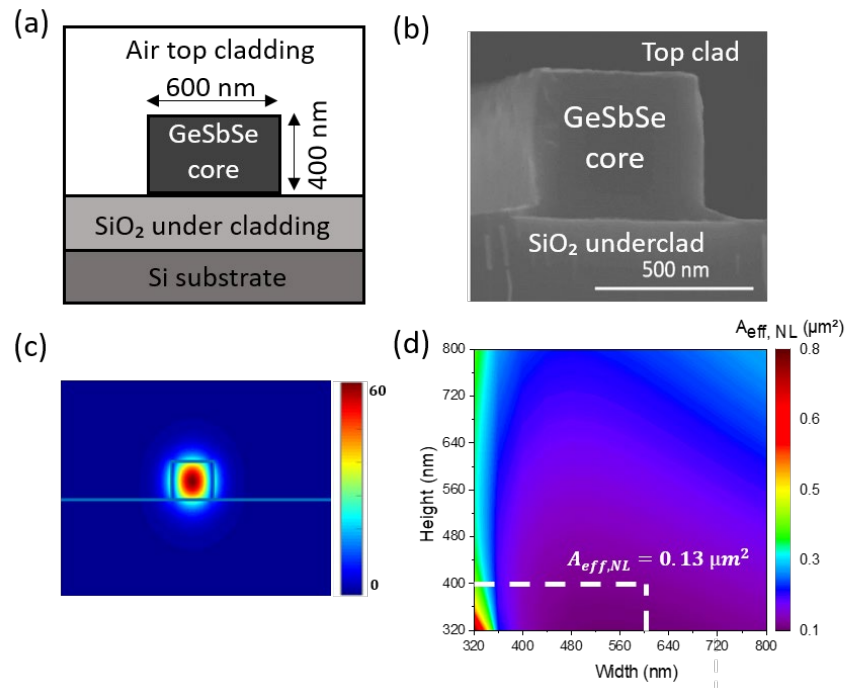


Fig. 1. (a) Schematic and (b) SEM micrograph of the cross-sectional structure of a GeSbSe-based ridge waveguide. (c) Theoretical field distribution of the fundamental TE-mode of the GeSbSe waveguide with a width of 600 nm and height of 400 nm. (d) Effective nonlinear area as a function of the width and the height of the GeSbSe waveguide.

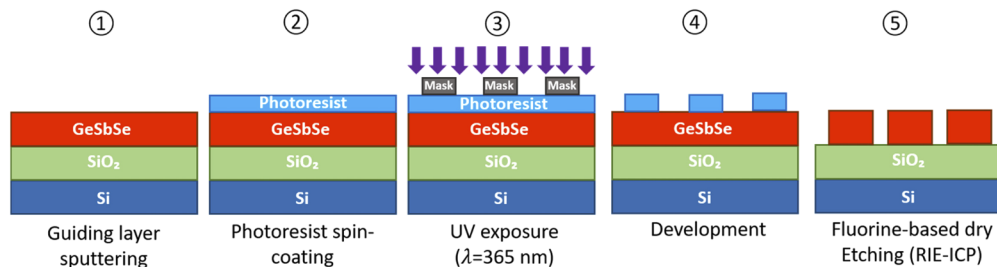


Fig. 2. Schematic of the ChG-ridge waveguide fabrication process.

3. Results and discussion

3.1. Linear optical characterization

Optical propagation losses for single mode GeSbSe ridge waveguides were measured using the cut-back method at a wavelength of 1550 nm. In this case, the measurements were performed on three sets of waveguides having five different lengths. In order to avoid successive cleaves of the sample, a photomask of “S” waveguides with different lengths was realized as showed in Fig. 3(a). The waveguides have the same number of bends whose the bending radius is fixed at 150 μm to avoid the bending losses. The results of these measurements are reported in Fig. 3(b). The uncertainties displayed in Fig. 3(b) are obtained from standard deviation of the transmission

measurements on these three waveguides for each propagation length. The propagation losses uncertainty comes from the fitting procedure. For a given GeSbSe ridge waveguide, propagation losses of $9.7 \pm 0.2 \text{ dB/cm}$, as well as coupling losses of 4.5 dB at each facet have been estimated from Fig. 3(b).

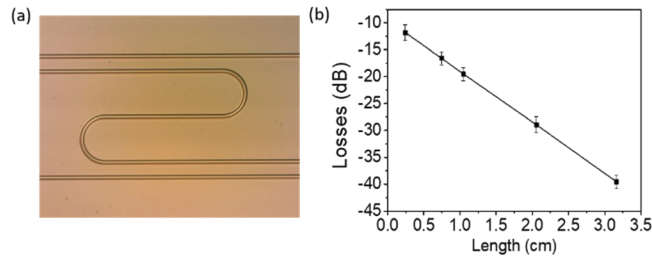


Fig. 3. (a) Representation of “S” waveguides with different lengths and (b) corresponding propagation losses measured at wavelength of 1550 nm for GeSbSe ridge waveguides.

In selenide ridge waveguides, the principal factors of propagation losses are: (a) the defects located at selenide confinement-guiding layer interfaces, (b) the side-walls roughness and (c) the volume scattering of selenide guiding layer [21,22]. Moreover, coupling losses stem from two sources namely mode mismatch losses (α_d) and Fresnel reflection losses (α_f). The mode mismatch losses come from the fact that the mode diameter of the micro-lensed fiber used for the injection of light in the waveguide [23] cannot be fully adapted to the diameter of the fundamental mode of the waveguide. The diameter of the fundamental mode of the waveguide is smaller than the mode diameter ($2.0 \pm 0.2 \mu\text{m}$) of the micro-lensed fiber. Fresnel losses correspond to the reflections at the interfaces between the optical chip and air. Taking into account these two sources of coupling losses (mode mismatch $\alpha_d \approx 3.5 \text{ dB}$ and Fresnel $\alpha_f \approx 0.5 \text{ dB}$), the theoretical coupling losses are about $\alpha_d + \alpha_f \sim 4 \text{ dB}$ per facet. From the fitting procedure of propagation losses, the mean experimental coupling losses are extrapolated at $L = 0 \text{ cm}$ and evaluated to $4.5 \pm 0.5 \text{ dB}$ per facet. The difference between the experimental and theoretical coupling losses could arise from the fact that the hand-cleaving of the sample was not ideally orthogonal to the waveguide axis.

3.2. Self-phase modulation

Self-phase modulation experiments were performed in the fabricated GeSbSe ridge waveguides using the experimental setup shown in Fig. 4 in order to determine their nonlinear propagation characteristics.

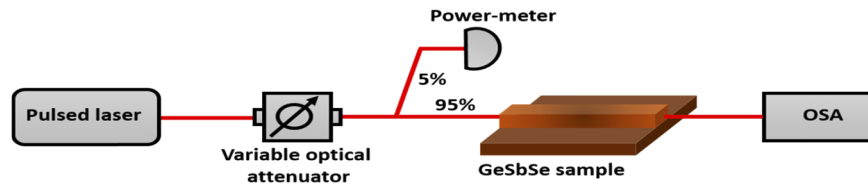


Fig. 4. Experimental setup used for the characterization of self-phase modulation in GeSbSe ridge waveguide. OSA: optical spectrum analyzer.

9.6 ps pulses with 19.3 MHz repetition rate at 1550 nm were coupled into the waveguide using a micro-lensed fiber mounted on a micro-alignment bench [23]. A variable optical attenuator was used to control the input power and a second micro-lensed fiber was used to couple the output of the waveguide to an optical spectrum analyzer. A 95/5 coupler connected to a power-meter was

inserted between the variable optical attenuator and the waveguide in order to measure the actual input pump power. The black curve in Fig. 5 represents the spectrum recorded at maximum input average power with set-up described in Fig. 4 without the component under test and after optimization of the micro-lensed fiber to micro-lensed fiber coupling. The total propagation length in single mode fibers (SMF) was kept below 4 meters for all measurements.

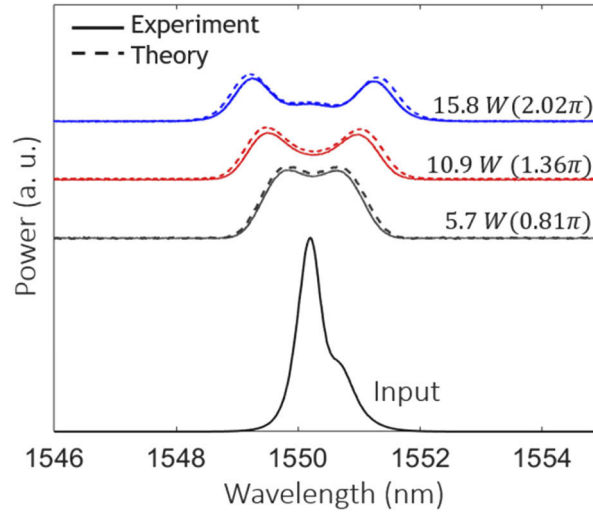


Fig. 5. Symmetric spectral broadening due to self-phase modulation within a 1.1 cm long GeSbSe ridge waveguide for different input peak power within the waveguide. The solid line represents the experiment and the dotted line is the theory.

This experiment aimed at demonstrating SPM so as to determine the nonlinear refractive index of the guiding layer of the GeSbSe ridge waveguide. For that, the output spectra of the pulses were measured for 7 different input peak powers ranging from 4.7 to 15.8 W. Examples of output spectra used to adjust the nonlinear refractive index are depicted in Fig. 5. A spectral broadening of optical pulses is observed, which is the signature of self-phase modulation occurring during pulse propagation along the GeSbSe ridge waveguide.

For a quantitative modelling of the experimental data, it is necessary to consider the combined effects of SPM and group-velocity dispersion (GVD) in the nonlinear GeSbSe ridge waveguide on spectral changes. Spectral broadening depends on several parameters: the nonlinear coefficient γ , the waveguide dispersion β_2 , the shape and the initial chirp C of the input pulse, the waveguide length L , and the waveguide attenuation. The nonlinear coefficient is expressed by $\gamma = (n_2 \times \omega_0) / (c \times A_{eff, NL})$, where ω_0 is the pump frequency, c is the speed of light and $A_{eff, NL}$ is the nonlinear effective area.

The modelling of the experimental data is performed thanks to a usual split-step algorithm [24]. The initial chirp of the pulse used in the experiment ($C = 0.7$) has been measured in a previous study [25], while the dispersion as shown in Fig. 6, is deduced from effective index calculation.

The effects of waveguide dispersion are clearly seen when comparing the material Se_6 dispersion to the GVD of the waveguide. The material Se_6 dispersion remains normal over the near-infrared wavelength range. While the total dispersion of the GeSbSe waveguide displays anomalous dispersion at a wavelength of 1550 nm ($D \sim 1055 \text{ ps.nm}^{-1}.\text{km}^{-1}$). On one hand, the dispersion effects can be quantified by the dispersion length which is defined as follows:

$L_D = \frac{T_0^2}{|\beta_2|}$ with T_0 is the input pulse width and β_2 is the waveguide dispersion. L_D is equal to 69 m in the case of GeSbSe waveguide with a width of 600 nm and height of 400 nm. Therefore, the dispersion effects are negligible since the chip length was chosen to be in the order of centimeters

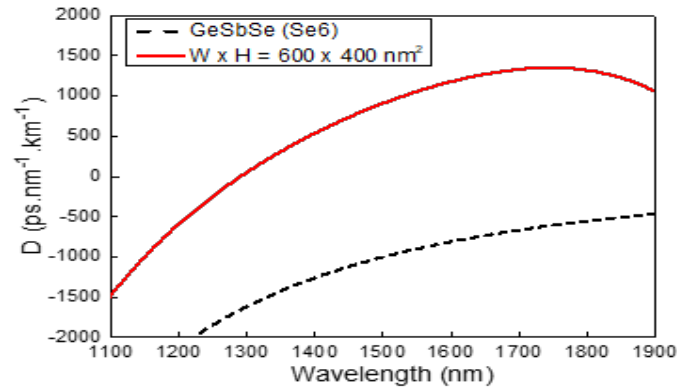


Fig. 6. The calculated material dispersion of the GeSbSe (Se_6) glass (dashed black line) and the simulated group velocity dispersion of the GeSbSe waveguide with a width of 600 nm and height of 400 nm (solid red line).

($L=1.1$ cm). On the other hand, the nonlinear effects are quantified by the nonlinear length which is defined as follows: $L_{NL} = \frac{1}{\gamma P}$ with γ is the nonlinear coefficient and P is the coupled pump power. Because of its small effective area in the order of μm^2 , the waveguide presents a small nonlinear length ($L_{NL} < 10^{-2}$ m). Hence, the nonlinear effects play a significant role during pulse propagation inside the waveguide since $L > L_{NL}$. Then, the condition $L > L_{eff} > L_{NL}$ should be respected so that the nonlinearities can overcome the limitations due to waveguide propagation loss value.

The nonlinear refractive index n_2 was adjusted to obtain the best agreement between the experimental and simulated spectra. Therefore, an average value of n_2 as well as a standard deviation (mean absolute difference between the experimental and the average n_2) can be determined from the 7 spectra. An average value for the Kerr nonlinear coefficient n_2 of 3.2×10^{-18} m^2/W and for its standard deviation of 1.3×10^{-18} m^2/W were estimated. The average n_2 is comparable to the value of n_2 ($2.0 \times 10^{-17} \pm 0.3 \times 10^{-17}$ m^2/W) reported in the literature [26]. This experiment, therefore, enables us to highlight self-phase modulation in ChG waveguides but also to determine the optical linear and nonlinear properties of the waveguides.

Self-broadening induces a SPM phase shift with a maximum at the center dip of the pulse. This maximum phase shift is defined as $\Phi_{max} = \gamma L_{eff} P$, where γ is the nonlinear coefficient defined above, $L_{eff} = [1 - \exp(-\alpha L)]/\alpha$ is the effective interaction length, calculated to be 0.4 cm and P is the coupled pump power [24]. Figure 7. shows the experimental nonlinear phase shift, exhibiting a linear relation with the pump power, and in good agreement with the simulated nonlinear phase shift that was calculated by using the average value for the Kerr nonlinear coefficient n_2 (3.2×10^{-18} m^2/W). From this figure, it is possible to deduce that the GeSbSe ridge waveguide presents a maximum nonlinear phase shift of 2.02π for a coupled peak power of 15.8 W.

Table 1 highlights some of the milestones reported for SPM demonstration with different ChG materials. The first demonstration of self-phase modulation in integrated ChG waveguides was achieved in 2002 by Bell laboratories [27]. A maximum nonlinear phase shift of π was obtained with a mode-locked laser delivering 380 fs short pulses. In 2006, a maximum nonlinear phase shift of 1.5π was obtained from a As_2S_3 rib waveguide pumped by 1.8 ps optical pulses at 1554.9 nm [28]. One decade later, the same maximum nonlinear phase shift was obtained also in a GeSbS ridge waveguide with $P_{peak} \sim 70 - 100$ W [29]. P_{peak} noted in Table 1 represents

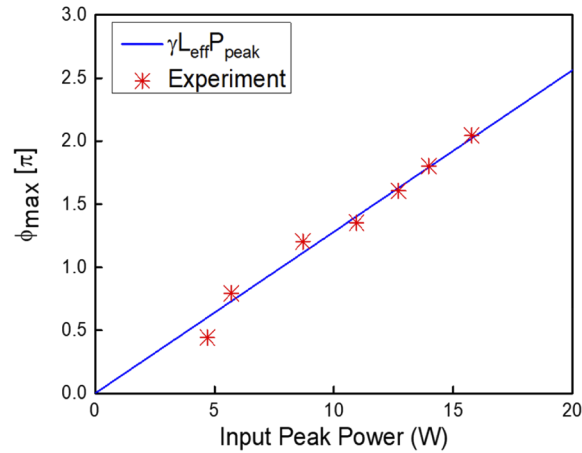


Fig. 7. Nonlinear phase shift versus coupled pump power. The blue line represents the maximum phase shift corresponding to the average n_2 ($3.2 \times 10^{-18} \text{ m}^2/\text{W}$) for 7 spectra and the red stars represent the maximum phase shift of each spectrum at a given pump power.

the coupled input peak power compensated for input fiber-waveguide coupling losses. We can conclude from Table 1, that the results displayed in Fig. 7 represent a significant improvement of maximum nonlinear phase shift reachable in ChG integrated waveguides. This is due to the reduction of the effective area which leads to an enhancement of the optical confinement in the nonlinear ChG core and to the high value of the nonlinear refractive index.

Table 1. Summary of nonlinear characteristics reported for chalcogenide waveguides.

Platform	Structure	$n_2(\text{m}^2/\text{W})$	$P_{peak}(\text{W})$	$\alpha(\text{dB}/\text{cm})$	$L(\text{cm})$	Φ_{max}	$\gamma L_{eff}(\text{W}^{-1})$
Ge _{0.25} Se _{0.75} [27]	Guiding layer	9.3×10^{-19}	1213	< 1.6	2.03	1.6π	< 0.005
	Confinement layer						
Si Substrate	Guiding layer	2.9×10^{-18}	53	0.3	5	1.5π	0.09
	Confinement layer						
	Si substrate						
Ge ₂₃ Sb ₇ S ₇₀ [29]	Guiding layer	3.71×10^{-18}	70 – 100	3.6	1.5	1.5π	0.06
	Confinement layer						
Si substrate	Guiding layer	3.2×10^{-18}	15.8	9.7	1.1	2.02π	0.4
	Confinement layer						
	Si substrate						

From left to right: nonlinear refractive index, coupled peak power, propagation loss, waveguide length, maximum nonlinear phase-shift.

3.3. Four-wave mixing

FWM characterization was also performed using the setup depicted in Fig. 8.

Two tunable CW lasers emitting at different wavelengths were used: the first one which is the most powerful is used as the pump wave while the second one plays the role of the signal wave. Each wave is amplified by an erbium-doped fiber amplifier (EDFA) and subsequently

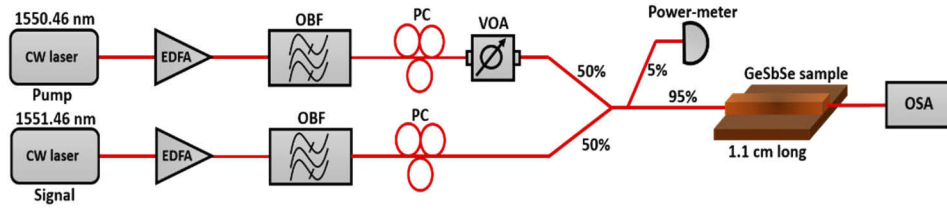


Fig. 8. Characterization setup used for the FWM experiments. OBF: optical band-pass filters, PC: polarization controllers, VOA: variable optical attenuator, EDFA: erbium-doped fiber amplifier.

filtered by a tunable optical band-pass filter (OBF). The filters were centered around the pump and signal wavelengths and employed to suppress the amplified spontaneous emission noise. On each arm, the polarization state can be adjusted by using a polarization controller (PC). A variable optical attenuator (VOA) was placed on the path of the pump laser to vary its power since laser operations were set at their maximum output powers. The pump and signal waves were coupled into the ChG waveguide using a fibered micro-lens with a mode radius of $2 \mu\text{m}$ and the output was collected from the waveguide with a second fibered micro-lens connected to either an optical spectrum analyzer or a power-meter. Before coupling into the waveguide, a 95/5 fiber coupler connected to a power-meter is placed in order to measure the pump and signal powers individually.

Figure 9(a) shows the measured FWM spectrum at the output of a 1.1 cm long GeSbSe waveguide with a $400 \times 600 \text{ nm}^2$ cross-section. A conversion efficiency of about -42.6 dB is obtained when a pump power of 28 mW and a signal power of 2.24 mW are coupled into the waveguide. The conversion efficiency is estimated from the FWM spectrum by using the following equation:

$$\eta_{FWM} = \frac{P_{i,output}}{P_{s,input}} \quad (2)$$

where $P_{s,input}$ and $P_{i,output}$ are the signal power at the waveguide input and the idler power at the waveguide output, respectively.

Figure 9(b) depicts the FWM conversion efficiency as a function of the coupled pump power where the theoretical FWM conversion efficiency follows a quadratic relation with the pump power under the assumption that the pump wave is high enough and undepleted by the nonlinear interaction:

$$\eta_{FWM} = (P_p \gamma L_{eff})^2 \text{sinc}^2 \left(\frac{KL_{eff}}{2} \right) \quad (3)$$

where P_p is the pump power at the waveguide input, γ is the nonlinear coefficient and L_{eff} is the effective interaction length of the waveguide of a length L and an attenuation coefficient α .

The total phase mismatch K represents the sum of the linear mismatch occurring as a result of the dispersive effects in the waveguide and the nonlinear mismatch arising from nonlinear effects. It is possible to notice from Fig. 9(b) that there is a satisfying agreement between the experimental and simulated η_{FWM} as a function of pump power. The last experimental point is placed lower than OSA detection limit ($\approx -63 \text{ dBm}$) because it corresponds to a pump power of $15.8 \text{ dBm} \approx 38 \text{ mW}$ for which the power density ($\approx 8.0 \times 10^6 \text{ W/cm}^2$) damaged optically the waveguide.

The main challenge in realizing significant four-wave mixing is to satisfy the phase-matching condition, which causes the idler intensity to build-up rather than to oscillate along the propagation path. Several methods can be used for realizing such phase-matching in practice. Alternatively, one can achieve an efficient four-wave mixing even if phase-matching is not perfect. To assess

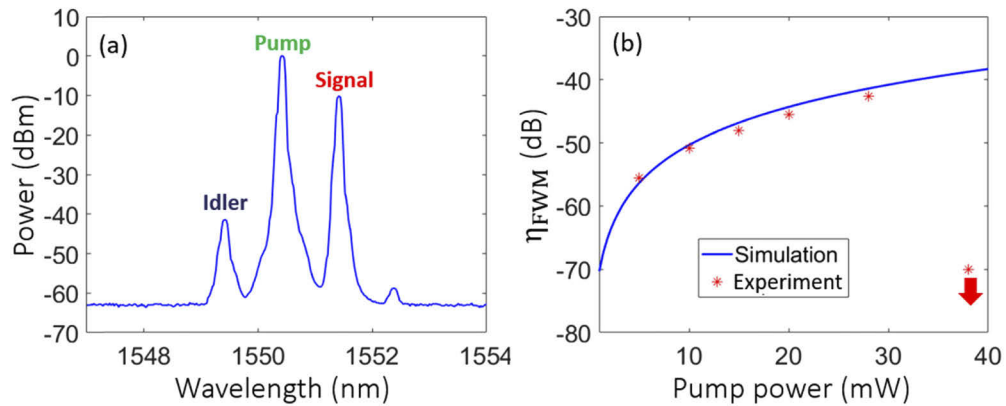


Fig. 9. (a) Optical output spectrum measured for a 1.1 cm long GeSbSe ridge waveguide (cross-sectional dimension: $400 \times 600 \text{ nm}^2$) with a coupled input pump power of 28 mW. (b) Measured output FWM conversion efficiency as a function of coupled input pump power for the waveguide of interest, the blue curve corresponds to the theoretical results and the red stars correspond to the experimental results. The phase mismatch was determined for a signal and a pump shifted by 1 nm. The last experimental point corresponds to the damaging point where the power density damaged optically the waveguide.

the tolerable amount of wave-vector mismatch over which the four-wave mixing effect can be observed, the FWM conversion efficiency as a function of pump-signal wavelength detuning for a GeSbSe ridge waveguide was characterized and plotted in Fig. 10. In this experiment, the pump wavelength was fixed at 1550.2 nm and the signal wavelength was varying till 1556.2 nm.

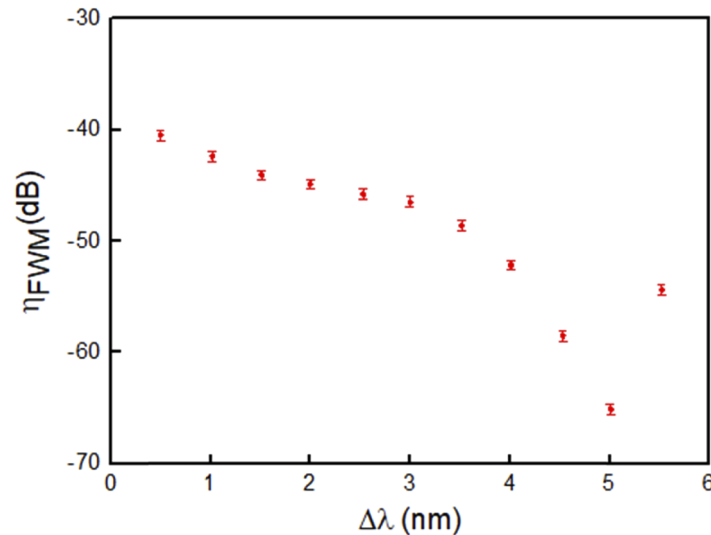


Fig. 10. Measured FWM conversion efficiency as a function of pump-signal wavelength detuning ($\Delta\lambda = \lambda_s - \lambda_p$) in GeSbSe ridge waveguide (cross-sectional dimension: $400 \times 600 \text{ nm}^2$).

For a GeSbSe ridge waveguide, the FWM conversion efficiency is almost flat over a detuning range from 0 to 3.5 nm. Then, it starts to dip once the signal wavelength is moving away from the pump wavelength. The FWM bandwidth, which is defined as the position of the first

minimum of the FWM conversion efficiency, is equal to 5 nm for a 1.1 cm long GeSbSe ridge waveguide. This value is limited by the relatively high material dispersion of GeSbSe. This waveguide was designed with intent to boost the effective nonlinear coefficient in order to achieve a FWM conversion efficiency as high as possible in the GeSbSe waveguide. However, to broaden the FWM bandwidth, the GeSbSe ridge waveguide needs also to be designed and optimized through dispersion engineering in a way that the pump wavelength coincides with zero-dispersion wavelength.

4. Conclusion and outlook

In conclusion, the use of Se₆ as guiding layer and SiO₂ as confinement layer was shown to improve the nonlinear parameter γ of the structure. By leveraging the high nonlinear parameter of the structure, SPM and FWM in a 1.1 cm long GeSbSe ridge waveguide were achieved. Spectral broadening induced by self-phase modulation with nonlinear maximum phase shift of $\Phi_{max} = 2.02 \pi$ for a peak power of $P_{peak} = 15.8 \text{ W}$ was obtained. By tailoring the waveguide dimensions in order to adjust the dispersion, such a spectral broadening can lead to a supercontinuum generation with octave-spanning bandwidths [30]. Four-wave mixing with conversion efficiency of $\eta_{FWM} = -42.6 \text{ dB}$ for a pump power of $P_{pump} = 28 \text{ mW}$ was achieved as well. By combining the high nonlinearities of Se₆ layer and the design of resonant photonic structures, the power required to generate FWM could be further decreased.

Funding

Lannion Tregor Communauté; Contrat Plan Etat Region (SOPHIE); Région Bretagne.

Acknowledgments

The sample fabrication was performed in the Centre Commun Lannion d'Optique (CCLO) –platform which is supported by the French RENATECH network.

Disclosures

The authors declare no conflicts of interest.

References

1. R. Salem, M. A. Foster, A. C. Turner, D. F. Geraghty, M. Lipson, and A. L. Gaeta, "Signal regeneration using low-power four-wave mixing on silicon chip," *Nat. Photonics* **2**(1), 35–38 (2008).
2. F. Da Ros, M. P. Yankow, E. P. da Saliva, M. Pu, L. Ottaviana, H. Hu, E. Semenova, S. Forchhammer, D. Zibar, M. Galili, K. Yvind, and L. K. Oxenløwe, "Characterization and optimization of a high efficiency AlGaAs-On-Insulator-Based wavelength converter for 64- and 256-QAM signals," *J. Lightwave Technol.* **35**(17), 3750–3757 (2017).
3. J. Wang, Q. Sun, and J. Sun, "All-optical 40 Gbit/s CSRZ-DPSK logic XOR gate and format conversion using four-wave mixing," *Opt. Express* **17**(15), 12555–12563 (2009).
4. W. Mathlouthi, H. Rong, and M. Paniccia, "Characterization of efficient wavelength conversion by four-wave mixing in sub-micron silicon waveguide," *Opt. Express* **16**(21), 16735–16745 (2008).
5. K. Dolgaleva, P. Sarrafi, P. Kultavewuti, K. M. Awan, N. Feher, J. S. Aitchison, L. Qian, M. Volatier, R. Arès, and V. Aimez, "Tunable four-wave mixing in AlGaAs nanowires," *Opt. Express* **23**(17), 22477–22493 (2015).
6. M. Pu, H. Hu, L. Ottaviano, E. Semenova, D. Vukovic, L. K. Oxenløwe, and K. Yvind, "Ultra-efficient and broadband nonlinear AlGaAs-on-insulator chip for low-power optical signal processing," *Laser Photonics Rev.* **12**(12), 1800111 (2018).
7. S. Serna, H. Lin, C. Alonso-Ramos, C. Lafforgue, X. Le Roux, K. A. Richardson, E. Cassan, N. Durbeuil, J. Hu, and L. Vivien, "Engineering third-order optical nonlinearities in hybrid chalcogenide-on-silicon platform," *Opt. Lett.* **44**(20), 5009–5012 (2019).
8. C. Koos, P. Vorreau, T. Vallaitis, P. Dumon, W. Bogaerts, R. Baets, B. Esembeson, I. Biaggio, T. Michinobu, F. Diederich, W. Freude, and J. Leuthold, "All-optical high-speed signal processing with silicon-organic hybrid slot waveguides," *Nat. Photonics* **3**(4), 216–219 (2009).

9. M. Ferrera, L. Razzari, D. Duchesne, R. Morandotti, Z. Yang, M. Liscidini, J. E. Sipe, S. Chu, B. E. Little, and D. J. Moss, "Low-power continuous-wave nonlinear optics in doped silica glass integrated waveguide structures," *Nat. Photonics* **2**(12), 737–740 (2008).
10. K. J. A. Ooi, D. K. T. Ng, T. Wang, A. K. L. Chee, S. K. Ng, Q. Wang, L. K. Ang, A. M. Agarwal, L. C. Kimerling, and D. T. H. Tan, "Pushing the limits of CMOS optical parametric amplifiers with USRN: Si₇N₃ above the two-photon absorption edge," *Nat. Commun.* **8**(1), 13878 (2017).
11. A. S. Kowligy, D. D. Hickstein, A. Lind, D. R. Carlson, H. Timmers, N. Nader, D. L. Maser, D. Westly, K. Srinivasan, S. B. Papp, and S. A. Diddams, "Tunable mid-infrared generation via wide-band four-wave mixing in silicon nitride waveguide," *Opt. Lett.* **43**(17), 4220 (2018).
12. J. L. Adam and X. Zhang, *Chalcogenide Glasses: Preparation, Properties and Applications* (Woodhead Publishing Limited, 2014).
13. B. J. Eggleton, B. Luther-Davies, and K. Richardson, "Chalcogenide photonics," *Nat. Photonics* **5**(3), 141–148 (2011).
14. F. Luan, M. D. Pelusi, M. R. E. Lamont, D. Choi, S. Madden, B. Luther-Davies, and B. J. Eggleton, "Dispersion engineered As₂S₃ planar waveguides for broadband four-wave mixing based wavelength conversion of 40 Gb/s signals," *Opt. Express* **17**(5), 3514–3520 (2009).
15. B. J. Eggleton, T. D. Vo, R. Pant, J. Schr, M. D. Pelusi, D. Yong Choi, S. J. Madden, and B. Luther-Davies, "Photonic chip based ultrafast optical processing based on high nonlinearity dispersion engineered chalcogenide waveguides," *Laser Photonics Rev.* **6**(1), 97–114 (2012).
16. S. Dai, F. Chen, Y. Xu, Z. Xu, X. Shen, T. Xu, R. Wang, and W. Ji, "Mid-infrared optical nonlinearities of chalcogenide glasses in Ge-Sb-Se ternary system," *Opt. Express* **23**(2), 1300–1307 (2015).
17. A. Gutierrez-Arroyo, E. Baudet, L. Bodiou, J. Lemaitre, I. Hardy, F. Fajjan, B. Bureau, V. Nazabal, and J. Charrier, "Optical characterization at 7.7 μm of an intergrated platform based on chalcogenide waveguides for sensing applications in the mid-infrared," *Opt. Express* **24**(20), 23109–23117 (2016).
18. P. Němec, M. Olivier, E. Baudet, A. Kalendová, P. Benda, and V. Nazabal, "Optical properties of (GeSe₂)_{100-x}(Sb₂Se₃)_x glasses in near-and middle-infrared spectral regions," *Mater. Res. Bull.* **51**, 176–179 (2014).
19. E. Baudet, A. Gutierrez-Arroyo, P. Němec, L. Bodiou, J. Lemaitre, O. De Sagazan, H. Lhermitte, E. Rinnert, K. Michel, B. Bureau, J. Charrier, and V. Nazabal, "Selenide sputtered films development for MIR environmental sensor," *Opt. Mater. Express* **6**(8), 2616–2627 (2016).
20. C. Koos, L. Jacome, C. Poulton, J. Leuthold, and W. Freude, "Nonlinear silicon-on-insulator waveguides for all-optical signal processing," *Opt. Express* **15**(10), 5976–5990 (2007).
21. J. Charrier, M. L. Anne, H. Lhermite, V. Nazabal, J. P. Guin, F. Charpentier, T. Jouan, F. Henrio, D. Bosc, and J. L. Adam, "Sulphide Ga_xGe_{25-x}Sb₁₀S_{65(x=0,5)} sputtered films: Fabrication and optical characterizations of planar and rib optical waveguide," *J. Appl. Phys.* **104**(7), 073110 (2008).
22. T. Tamir, *Guided-wave Optoelectronics* 26, (Springer, 1988), Chap. 6.
23. S. D. Le, E. Delcourt, P. Girault, A. Gutierrez-Arroyo, P. Azuelos, N. Lorrain, L. Bodiou, L. Poffo, J. M. Goujon, Y. Dumeige, I. Hardy, P. Rochard, J. Lemaitre, P. Pirasteh, M. Guendouz, T. Chartier, L. Quételet, S. Claudot, J. Charrier, and M. Thual, "Study of optimized coupling based on micro-lensed fibers for fibers and photonic integrated circuits in the framework of telecommunications and sensing applications," *Commun. Phys.* **26**(4), 325–334 (2017).
24. G. P. Agrawal, *Nonlinear Fiber Optics* (Academic Press, 1989).
25. D. M. Nguyen, T. N. Nguyen, T. Chartier, and M. Thual, "Accuracy improvement in the measurement of the non-linear coefficient of optical fibers based on self-phase modulation," *Fiber Integr. Opt.* **29**(4), 225–238 (2010).
26. T. Kuriakose, E. Baudet, T. Halenkovič, M. R. M. Elsayy, P. Němec, V. Nazabal, G. Renversez, and M. Chauvet, "Measurement of ultrafast optical kerr effect of Ge-Sb-Se chalcogenide slab waveguide by the beam self-trapping technique," *Opt. Commun.* **403**, 352–357 (2017).
27. S. Spälter, H. Y. Hwang, J. Zimmermann, G. Lenz, T. Katsufuji, S.-W. Cheong, and R. E. Slusher, "Strong self-phase modulation in planar chalcogenide glass waveguides," *Opt. Lett.* **27**(5), 363–365 (2002).
28. V. G. Ta'eed, M. Shokooh-Saremi, L. Fu, I. C. M. Littler, D. J. Moss, M. Rochette, B. J. Eggleton, Y. Ruan, and B. Luther-Davies, "Self-phase modulation-based integrated optical regeneration in chalcogenide waveguides," *IEEE J. Sel. Top. Quantum Electron.* **12**(3), 360–370 (2006).
29. J. W. Choi, Z. Han, B. Sohn, G. F. R. Chen, C. Smith, L. C. Kimerling, K. A. Richardson, A. M. Agrawal, and D. T. H. Tan, "Nonlinear characterization of GeSbS chalcogenide glass waveguide," *Sci. Rep.* **6**(1), 39234 (2016).
30. Q. Du, Z. Luo, H. Zhong, Y. Zhang, Y. Huang, T. Du, W. Zhang, T. Gu, and J. Hu, "Chip-scale broadband spectroscopic chemical sensing using an integrated supercontinuum source in a chalcogenide glass waveguide," *Photonics Res.* **6**(6), 506–510 (2018).